

Tuning the Electronic Properties of Two-Dimensional Lepidocrocite Titanium Dioxide Based Heterojunctions

Kati Asikainen^{†,*}, Matti Alatalo[†], Marko Huttula[†], and S. Assa Aravindh^{†,*}

[†]*Nano and Molecular Systems Research Unit, University of Oulu, FI-90014, Finland*

E-mail: Kati.Asikainen@oulu.fi; Assa.SasikalaDevi@oulu.fi

Abstract

Two-dimensional (2D) heterostructures reveal novel physicochemical phenomena at different length scales, that are highly desirable for technological applications. We present a comprehensive density functional theory study of van der Waals (vdW) heterostructures constructed by stacking 2D TiO_2 and 2D MoSSe monolayers to form TiO_2 -MoSSe heterojunction. The heterostructure formation is found to be exothermic, indicating stability. We find that by varying the atomic species at the interfaces the electronic structure can be considerably altered, due to the differences in charge transfer, arising from the inherent electronegativity of the atoms. We demonstrate that the heterostructures possess a type II or type III band alignment, depending on the atomic termination of MoSSe at the interface. The observed charge transfer occurs from MoSSe to TiO_2 . Our results suggest that Janus interface enables the tuning of electronic properties, providing understanding of the possible applications of the TiO_2 -MoSSe heterostructure.

Introduction

Titanium dioxide (TiO_2) is one of the premier materials in various applications including e.g. photovoltaic cells,^{1,2} photocatalysis^{3,4} and batteries.^{5,6} Excellent chemical stability, eco-friendliness, and low cost are the favorable factors of TiO_2 , but possible drawbacks that limit the performance include large band gap of bulk phases and fast recombination of electron and hole pairs. Various strategies such as doping, tuning of morphology, and constructing heterostructures with different lattice matching semiconductors have been successfully employed in order to overcome the above shortcomings. Another strategy to enhance the activity of semiconductors is to construct low dimensional materials that provide many active surface sites compared to their bulk counterparts. Because of this advantage, two-dimensional (2D) materials are gathering wide attention compared to their 3D phases.⁷ 2D TiO_2 with lepidocrocite-like structure has been synthesized through exfoliation by means of soft-chemical procedures by Sasaki et.al.,⁸ and later theoretically confirmed to be thermodynamically stable.⁹ Experimentally synthesized 2D Lepidocrocite-type TiO_2 possesses a large band gap (3.8 eV) due to the quantum confinement.¹⁰ Despite this shortcoming, it has been shown to be a suitable candidate for both hydrogen and oxygen evolution reactions (HER and OER), with the possibility of improving the photocatalytic performance via transition-metal doping.^{11,12}

For application purposes, heterojunctions constructed by stacking two or more 2D monolayers are promising, as they provide ample opportunities for band bending, due to the spatial variation of the Fermi level of the semiconductors constituting the heterojunction. The three most conventional band alignments are type I (straddling gap), type II (staggered gap) and type III (broken gap), each of these are beneficial for the development of materials for different applications. Type I band alignment is useful in optical devices such as light-emitting diodes (LEDs)¹³ as it leads to charge carrier accumulation in one location and high recombination rate under light irradiation. By providing spatial separation of electrons and holes into different locations, thus reducing the recombination rate, type

II band alignment is desirable in photocatalytic applications¹⁴ and photovoltaic cells.¹⁵ Finally, the type III band alignment allows tunneling of electrons from one material to another, becoming favorable for tunnel field-effect transistors (TFETs).¹⁶ Multiple studies have demonstrated vdW heterostructures and the formation of a heterojunction to improve the light harvesting into visible light, and enable charge transfer across the interface,¹⁷⁻²¹ leading to superior properties, and broadening the applications of 2D materials.

2D Janus materials are a novel class of materials, extensively studied recently due to the multitude of opportunities in device applications. They were experimentally synthesized for the first time in 2017, by breaking the out of plane structural symmetry of MoS₂, and replacing S atoms by Se atoms on one side.²² The name Janus originates from the two faced Roman god Janus, and the MoSSe Janus material consists of two different chalcogen atoms (S and Se) on either side of a Mo atom sandwiched in the middle. Thermodynamic stability of MoSSe is well established from phonon band structure analysis,²³ and therefore it is worthwhile to investigate if MoSSe can form heterojunctions with other lattice matching semiconductors. Even though the synthesis of MoSSe kick-started the research interest in these materials, recent studies also focus on other possible materials, such as PtSSe, WSeTe and many others,²⁴⁻²⁷ for various applications.

Previously, 2D lepidocrocite-type TiO₂-based vdW heterostructures containing GaSe and MoS₂ have been investigated for enhancing the performance of the isolated TiO₂ monolayer.^{28,29} However, to the best of our knowledge, a vdW heterostructure of 2D TiO₂ and 2D MoSSe has not yet been studied. These materials have fairly similar lattice parameters ($a = 3.00 \text{ \AA}$ and $b = 3.80 \text{ \AA}$ for 2D TiO₂,³⁰ and $a = b = 3.24 \text{ \AA}$ for 2D MoSSe²²) which is essential in creating small lattice-mismatch heterostructures. Strict lattice-matching may not be necessary³¹ but a large mismatch can affect the stability and performance of the heterostructures. Therefore, in this work, we investigate the structural and electronic properties of 2D TiO₂/MoSSe vdW heterostructure by employing first principles calculations. The study was started by optimizing the heterostructures.

The electronic structure was examined through the band structure and density of states and further, charge density analysis, planar-averaged electrostatic potential, and work function were calculated to obtain more insight into charge transport properties in the heterostructures.

Computational methodology

We performed first principles density functional theory (DFT) calculations to investigate vdW heterostructure of TiO₂ and MoSSe using the plane wave code VASP (Vienna Ab initio Simulation Package).³²⁻³⁵ The projected augmented wave (PAW) based pseudopotentials with plane wave basis sets were employed.³⁶ A kinetic energy cutoff of 520 eV was employed to include the plane waves in the basis set. The exchange-correlation potential was described by generalized gradient approximation (GGA) in the Perdew-Burke-Ernzerhof (PBE) scheme.³⁷ Since GGA is inadequate to describe the on-site Coulomb interaction between localized d and f electrons, we applied DFT+U to treat the localized Ti 3d electrons in order to obtain more realistic electronic properties. We added a correction of $U_{\text{eff}} = 4.5 \text{ eV}$ ($U = 4.5, J = 0$)³⁸ according to the scheme of Dudarev *et al.*³⁹ Van der Waals interactions between TiO₂ and MoSSe were included with the DFT-D2 method of Tkatchenko and Scheffler.⁴⁰ The Brillouin zone was sampled according to the Monkhost-Pack scheme⁴¹ and Gaussian smearing with a width of 0.05 eV was used. The convergence threshold for energy and forces were set to 10^{-6} eV and $0.001 \text{ eV \AA}^{-1}$, respectively. We used VESTA⁴² for visualization and VASPKIT⁴³ for post-processing the outputs of the DFT-calculations.

The initial structure of 2D TiO₂ was constructed according to the structural parameters reported in Ref.⁹ 2D MoSSe unit cell was created from the hexagonal unit cell of MoS₂ by replacing one S interface by Se. To sample the 1st Brillouin zone, k-point meshes of $6 \times 6 \times 1$ and $5 \times 5 \times 1$ were used for TiO₂ and MoSSe monolayers, respectively. The vdW heterostructures were constructed via stacking pristine TiO₂ and MoSSe monolayers, with

a rectangular supercell of sizes 1x3x1 and 1x2x1, respectively, along the vertical direction. The size of the rectangular unit cell of MoSSe was $a = 3.25 \text{ \AA}$ and $b = 5.64 \text{ \AA}$ (Figure S1). Due to the lattice mismatch, the constructed heterostructure forms a Moiré pattern.⁴⁴ Resulting from this, the stacking configuration is not the same in all regions but in a long range the periodicity appears. Li *et al.* have investigated a few stacking configurations of 2D lepidocrocite-type TiO₂ and 2D MoS₂. They found that the Moiré pattern, in which the zigzag direction of MoS₂ and the in-plane edge of TiO₂ with a smaller lattice parameter were aligned in the same direction, was the most stable according to adsorption energies calculated with respect to the interlayer distance.²⁹ Therefore, in this work we focused on this particular stacking configuration of 2D TiO₂ and 2D MoSSe (Figure S2). The lattice mismatch in the x- and y-directions was calculated as $\frac{(a-b)}{a} \times 100\%$, where a and b denote the lattice parameter of TiO₂ and MoSSe monolayers, respectively. This resulted in a lattice mismatch of 7.17 % in the x-direction and -0.08 % in the y-direction. In the y-direction, the effect of strain is negligible. A vacuum with a thickness of around 23 Å was added along z-direction to both interfaces to avoid correlation between periodic images. Because Mo-layer is sandwiched by two distinct chalcogen layers, S-layer and Se-layer, heterostructures with two different interfaces can be constructed: TiO₂-MoSSe (S atoms at the interface) and TiO₂-MoSeS (Se atoms at the interface). A k-point sampling of $18 \times 5 \times 1$ within the Monkhorst-Pack scheme was adopted.

Results and discussion

Before building the heterostructures, we investigated a freestanding 2D TiO₂ and MoSSe monolayers. The optimized geometries of the monolayers are shown in Figure S3. The optimized lattice parameters of TiO₂ were $a = 3.03 \text{ \AA}$ and $b = 3.77 \text{ \AA}$, and Ti-O distances were 1.85-2.22 Å (Figure S4). For MoSSe, we found lattice parameters of $a = b = 3.25 \text{ \AA}$. Mo-S, Mo-Se, Se-Se and S-S distances were 2.42 Å, 2.54 Å, 3.26 Å and 3.26 Å, respectively.

Our calculated lattice parameters are in agreement with existing research.^{28,45} Furthermore, we calculated the electronic band structure of the monolayers (Figure S5). Using the GGA functional, we found a direct band gap of 2.76 eV at Γ for TiO_2 .^{9,46} Applying the Hubbard correction the band gap of 3.30 eV was obtained which compares better with the experimental value of 3.8 eV¹⁰ and previously obtained value using the GGA+U.²⁸ Previously, higher-level approximations have also been applied to calculate the electronic structure. Using the HSE06 functional Li *et al.*²⁹ obtained a band gap of 3.87 eV which is extremely close to the experimental value. Besides, Wang *et al.*⁴⁷ have obtained a band gap of 5.97 eV using the GW approximation, and Zhou *et al.*⁴⁶ have calculated the band gap using the G_0W_0 +BSE, and reported a band gap of 5.3 eV. Therefore, it can be seen that we need to be careful while comparing different approaches, as over and under-estimation of band gaps can be seen across different functionals. Calculated direct band gap of 1.59 eV for MoSSe is closer to the experimental band gap of 1.68 eV²² and reported results using the GGA functional.^{45,48}

The optimized structures of the $\text{TiO}_2/\text{MoSSe}$ and $\text{TiO}_2/\text{MoSeS}$ heterostructures are shown in Figure 1. The obtained lattice constants of the above two heterostructures were $a = 3.11 \text{ \AA}$ and $b = 11.18 \text{ \AA}$ after the optimization. The interlayer distance between the monolayers was 2.75 \AA in the $\text{TiO}_2/\text{MoSSe}$ and 2.90 \AA in the $\text{TiO}_2/\text{MoSeS}$. These values fall within the optimal range of vdW interaction as discussed by Wang *et al.*⁴⁹ and Pushkarev *et al.*⁵⁰ The smaller interlayer distance in the $\text{TiO}_2/\text{MoSSe}$ may be attributed to a larger covalent radius of the Se atoms than the S atoms, resulting in a larger spacing between the monolayers.^{51,52} Interlayer distances smaller than 3 \AA have also been reported in previous investigations on TiO_2 -based heterostructures^{28,29,53} and other vdW heterostructures as well.⁵⁴⁻⁵⁶ To estimate the stability of the heterostructures we calculated the formation energies using the equation

$$E_F = E_{\text{Heterostructure}} - E_{\text{TiO}_2} - E_{\text{MoSSe}}, \quad (1)$$

where $E_{\text{Heterostructure}}$ is the total energy of the heterostructure and E_{TiO_2} and E_{MoSSe} are the total energies of the TiO_2 and MoSSe monolayers. The calculated formation energies of -5.52 eV and -5.50 eV for $\text{TiO}_2/\text{MoSSe}$ and $\text{TiO}_2/\text{MoSeS}$, respectively, indicated that the vdW heterostructures are energetically favorable. Previously, Ahmad et al.⁵⁷ have reported a low binding energy of -5.97 eV for $\text{InSe}/\text{PdSe}_2$ heterostructure. Together with the interlayer distances the results suggest high stability for the heterostructure and stronger physical interaction between the monolayers.^{50,51,55,56} Of the two heterostructures the $\text{TiO}_2/\text{MoSSe}$ is slightly more stable than the $\text{TiO}_2/\text{MoSeS}$.

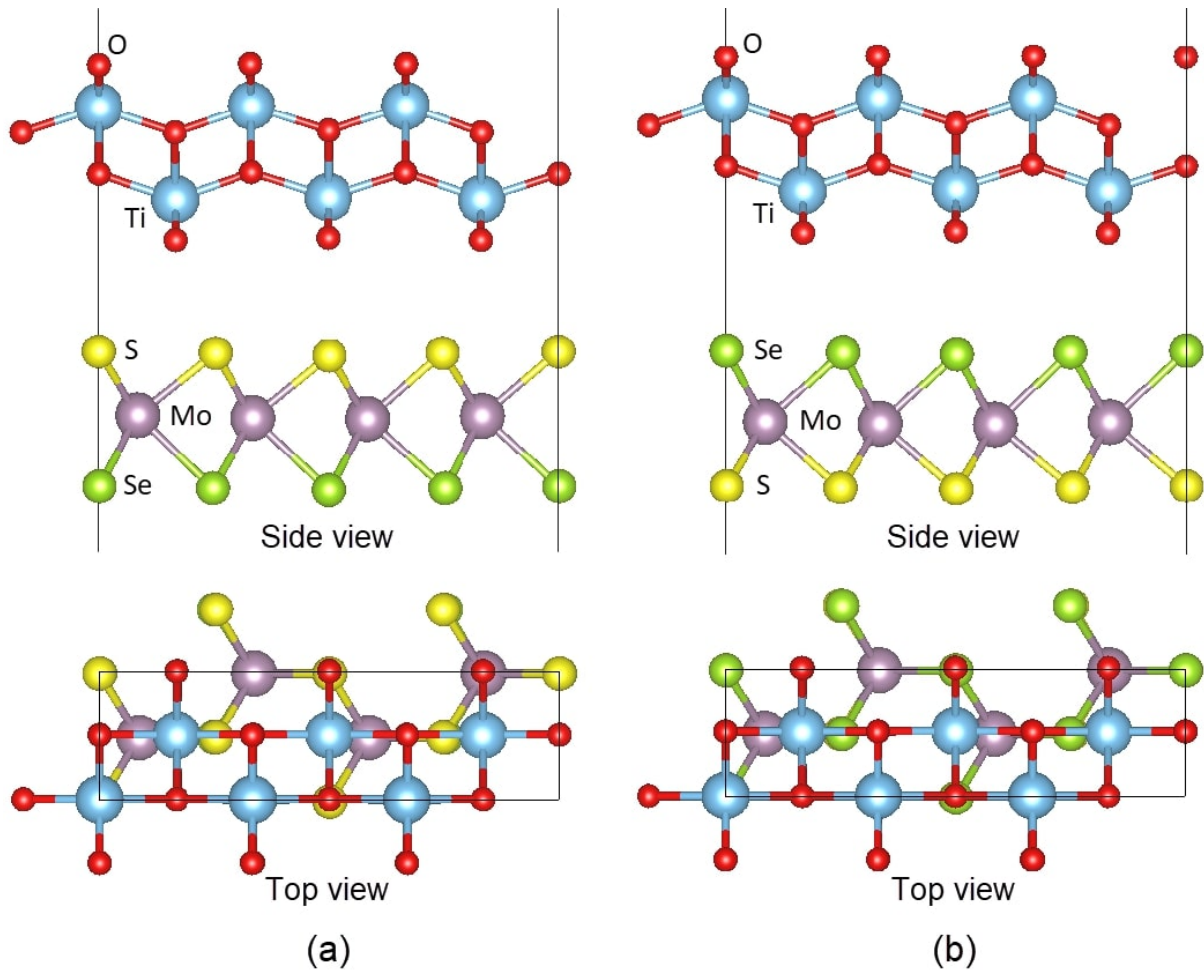


Figure 1: Side view (along y-direction) and top view (along z-direction) of the optimized a) $\text{TiO}_2/\text{MoSSe}$ and b) $\text{TiO}_2/\text{MoSeS}$ heterostructures. The colour coding of the atoms is the same here and elsewhere.

After investigating the electronic structure of the monolayers, we extended the same

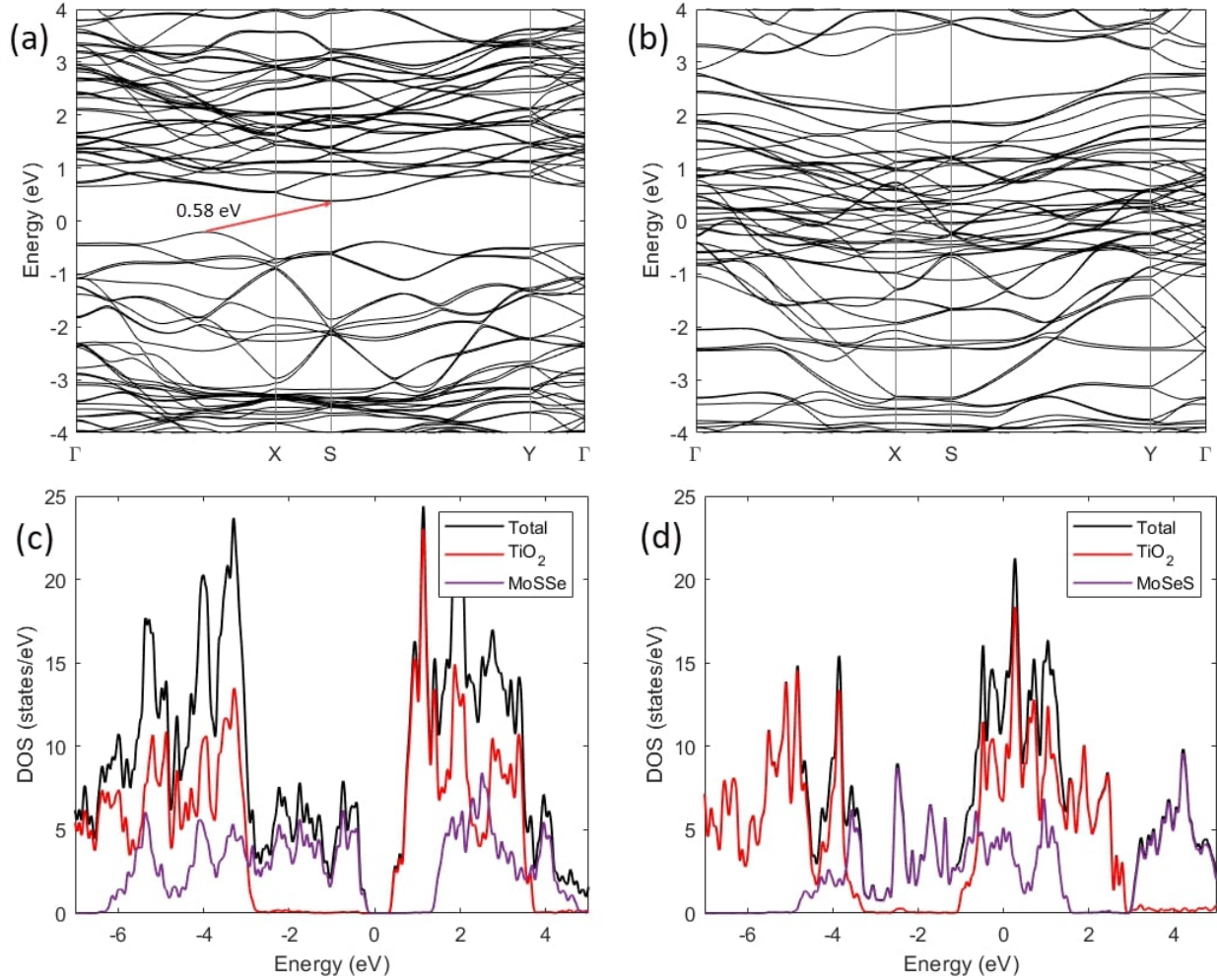


Figure 2: Band structure and density of states of the $\text{TiO}_2/\text{MoSSe}$ (a and c) and $\text{TiO}_2/\text{MoSeS}$ (b and d) heterostructures using the GGA+U functional. The indirect band gap is indicated with a red arrow in a).

calculations for the heterostructures. Figure 2 shows the band structure and density of states (DOS) of the heterostructures. The formation of the vdW heterostructure led to a significant left-shift of the density of states of TiO_2 , towards the lower energy regions. The $\text{TiO}_2/\text{MoSSe}$ heterostructure was found to be an indirect-band gap semiconductor (Figure 2a). The valence band maximum (VBM) was located between Γ and X and the conduction band minimum (CBM) at S, resulting in a band gap of 0.58 eV. This is evidently lower than the band gap of the freestanding monolayers, facilitating electron excitation. The quasi-direct band gap was located between S and Y and it was 0.84 eV. It can be

seen from the DOS that the top of the valence band (VB) is dominated by the MoS₂ monolayer while the bottom of the conduction band (CB) is contributed by TiO₂ (Figure 2c). This indicated a type II band alignment between TiO₂ and MoS₂, allowing the charge transfer from MoS₂ to TiO₂. To confirm this, we have calculated the decomposed charge densities of the VBM and CBM which showed that the VBM is constituted from the states of MoS₂ while the CBM is contributed by TiO₂ (Figure S6a and S6b). Consequently, the charge density is completely separated, making it possible to separate the photogenerated electrons and holes in the heterostructure. This particular band alignment is extremely desired for photocatalytic applications.^{14,20} The band structure revealed the formation of metallic states in the TiO₂/MoS₂ due to the overlapping of VB of MoS₂ with the CB of TiO₂ (Figure 2b). Both the VBM and CBM of TiO₂ lied below the Fermi level, and the VBM and CBM of MoS₂ above the Fermi level (Figure 2d), that is, the highest VB edge of MoS₂ was located in higher energy level than the lowest CB edge of TiO₂ (Figure 2d). This suggested that the TiO₂/MoS₂ heterostructure possesses a broken gap type-III band alignment. The broken gap enables a band-to-band tunneling (BTBT) mechanism between TiO₂ and MoS₂.¹⁷ Thus, electrons in the VB of MoS₂ can directly tunnel to the CB of TiO₂ without light absorption or emission. The decomposed charge density plots in Figure S6c and S6d showed that the VBM is contributed by MoS₂ while the CBM is distributed around both monolayers. In TiO₂ the CBM mainly concentrated on the atoms at the interface in MoS₂, the charge density distributed around all atoms of MoS₂. Electrons from VBM of MoS₂ can be excited by photons to the CBM of MoS₂. Simultaneously, the band alignment allows electron tunneling from the VBM of MoS₂ to the CBM of TiO₂, explaining the observed decomposed charge density distribution. We found a large tunneling window (energy difference between the VB of MoS₂ and CB of TiO₂) of around 2.78 eV, indicating greater tunneling probability for electrons. Due to the formation of type III band alignment associated with metallic character, the TiO₂/MoS₂ heterostructure can be a potential candidate for tunneling devices, such as TFETs and Esaki diodes.^{16,58} The

particular band alignment can induce a negative differential resistance in heterostructures which is favorable especially in TFETs.^{59,60} The contributions of each element to the density of states are shown in Figure S7.

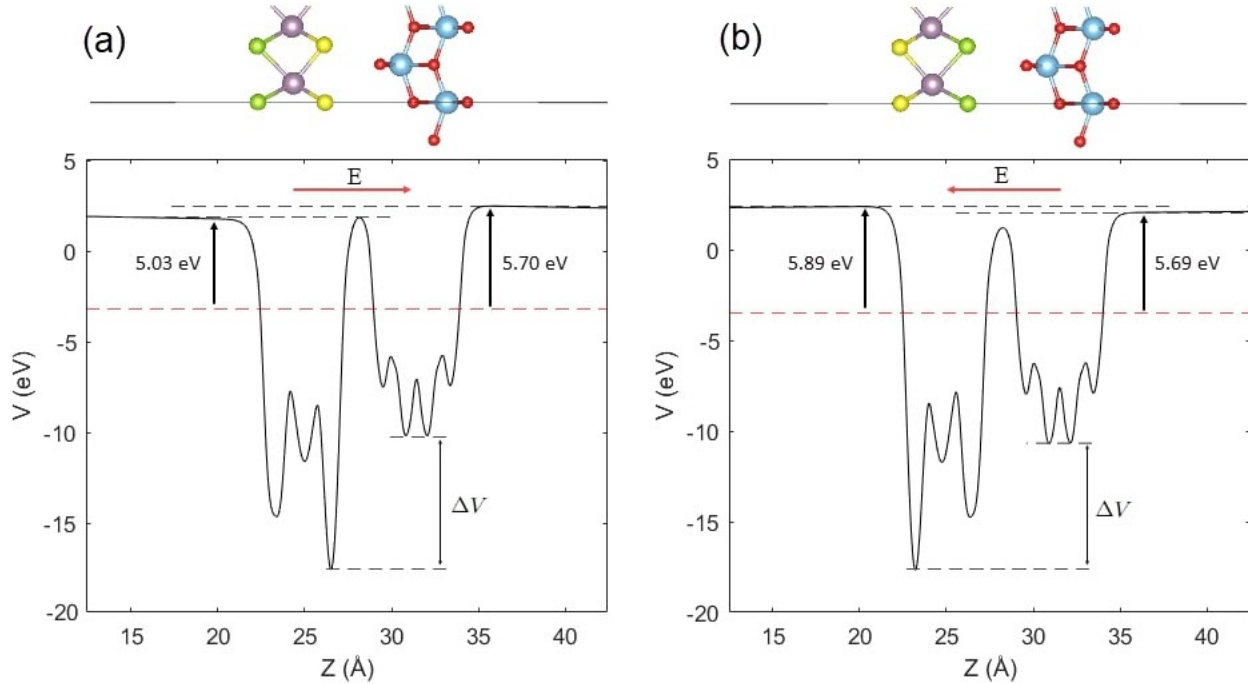


Figure 3: Electrostatic potential of the a) $\text{TiO}_2/\text{MoSSe}$ and b) $\text{TiO}_2/\text{MoSeS}$ heterostructures. The Fermi level is indicated with dashed red line, and the direction of built-in electric field E with red arrow. The potential drop of the heterostructures across the interface is represented by ΔV .

We calculated the work function Φ using the equation

$$\Phi = E_{\text{vac}} - E_{\text{F}}, \quad (2)$$

where E_{vac} and E_{F} represent the vacuum level and Fermi level, respectively. The calculated work function of TiO_2 was 8.60 eV (Figure S8a) whereas MoSSe exhibited two different work functions: 5.20 eV at the Se termination and 5.79 eV at the S termination, due to the intrinsic polarization (Figure S8b). This resulted in an electrostatic potential difference of 0.59 eV between the terminations. These are in line with previous work.^{18,61} Because the work function of both the S and Se terminations of MoSSe are smaller than that of

TiO₂, the results suggest electron flow from MoSSe to TiO₂ when combining the two monolayers until thermodynamic equilibrium is reached. We found that the formation of the heterostructures significantly decreased the work function of TiO₂. Moreover, because of the electrostatic potential difference between the terminations of MoSSe, the work functions of the two surfaces of TiO₂/MoSSe and TiO₂/MoSeS were found to be different. The planar-averaged electrostatic potential of the heterostructures along the z-direction is shown in Figure 3. The work functions at the TiO₂ and MoSSe surfaces were 5.70 eV and 5.03 eV in the TiO₂/MoSSe (Figure 3a), and 5.69 eV and 5.89 eV in the TiO₂/MoSeS (Figure 3b), respectively. Interestingly, the heterostructure possesses a lower work function at the MoSSe surface when the S termination is placed at the interface, whereas placing the Se termination at the interface results in a lower work function at the TiO₂ surface. This has also been observed in other 2D MoSSe-based heterostructures.⁶²⁻⁶⁴ This may be explained by the intrinsic polarization observed in pristine MoSSe. Since S atoms have larger electronegativity, electrons tend to accumulate in the S layer of MoSSe, increasing the work function and potential energy (Figure S8b). Thus, the direction of the intrinsic dipole moment is from S to Se. When combining MoSSe with TiO₂, this property appears to be preserved, showing that the intrinsic polarization of MoSSe takes up a significant role in giving rise to a polarization in the heterostructures. Resulting from the different work functions at the two surfaces, there exists an electrostatic potential difference $\Delta\phi$ of 0.67 and 0.2 eV in the TiO₂/MoSSe and TiO₂/MoSeS, respectively, which induces a built-in electric field at the interface of the heterostructures,^{18,19,65} pointing from MoSSe to TiO₂ in the TiO₂/MoSSe, and from TiO₂ to MoSSe in the TiO₂/MoSeS. Moreover, the electrostatic potential of TiO₂ was deeper than that of MoSSe, resulting in a potential drop ΔV across the interface. The potential drop was 7.37 eV in the TiO₂/MoSSe and 6.95 eV in the TiO₂/MoSeS. This gradient, directed from MoSSe to TiO₂, was attributed to the difference in the electronegativity of oxygen (3.44), and S (2.58) and Se (2.55), and it can further facilitate the charge separation of electrons and holes.^{68,69}

A schematic diagram in Figure 4 shows the work functions and band edge positions of the monolayers and the heterostructures with respect to the vacuum level. The band alignment of materials is essential in designing materials for practical applications. The TiO₂/MoSSe heterostructure retained the band ordering of the two monolayers, resulting in a type II band alignment, and the band gap energies of the monolayers were only slightly affected by the formation of the heterostructure. We found a band gap of 3.26 eV for TiO₂ and 1.58 eV for MoSSe. In the TiO₂/MoSeS the band gap of TiO₂ and MoSSe did not overlap which is known as broken gap. The energy difference between the VB and CB of TiO₂ and the VB and CB of MoSSe were reduced to 2.43 eV and 1.44 eV, respectively. This shows that Se termination at the interface affects more significantly the band gap energies of the monolayers in the heterostructure.

To further identify the charge transfer in the heterostructures, we have calculated the charge density difference in Figure 5 as $\Delta\rho = \rho_{\text{Heterostructure}} - \rho_{\text{TiO}_2} - \rho_{\text{MoSSe}}$ where $\rho_{\text{Heterostructure}}$, ρ_{TiO_2} and ρ_{MoSSe} are the charge densities of the heterostructure, TiO₂ monolayer and MoSSe monolayer, respectively. In the TiO₂/MoSSe, the charge redistribution was localized at the interface. In the TiO₂ the O atoms at the interface mainly experienced changes in the charge density, whereas the changes were more obvious in the S termination of MoSSe. The strongest interaction occurred between the nearest O and S atoms where the charge redistribution is significant. The results are comparable with the study conducted by Y. Li *et al.* although different exchange-correlation functional were used in the calculations.²⁹ In the TiO₂/MoSeS, notable charge re-arrangement occurred around the interface, which also extended to the outer side of both monolayers. The blue isosurface at the S and Se terminations showed that MoSSe contributes electrons to TiO₂. In order to quantify the amount of the charge transfer in the heterostructures, we performed the Bader analysis.⁷⁰ According to the analysis, a charge of 0.038 *e* and 0.020 *e* per unit cell was transferred from MoSSe to TiO₂ in the TiO₂/MoSSe and TiO₂/MoSeS, respectively. Thus, after constructing the heterostructures, n-type doping is realized in TiO₂ while p-type doping in MoSSe. The

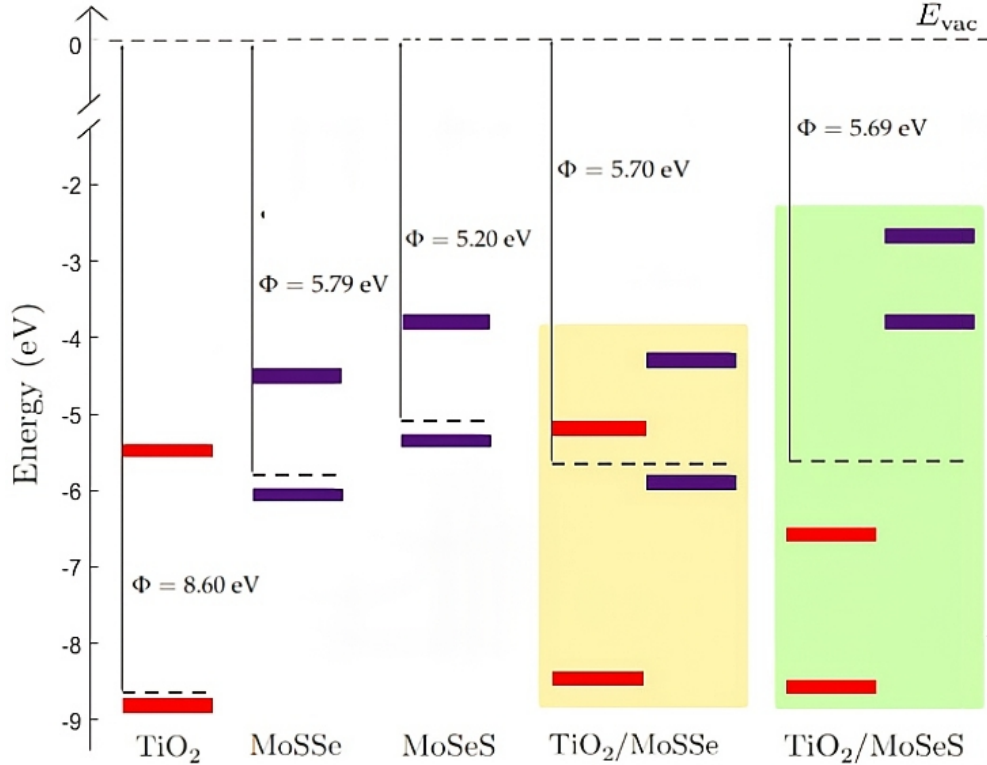


Figure 4: Band alignment and work function of the freestanding TiO_2 and MoS_2e monolayers, and $\text{TiO}_2/\text{MoS}_2\text{e}$ and $\text{TiO}_2/\text{MoSeS}$ heterostructures. The band positions of TiO_2 are depicted in red and MoS_2e in purple. The band positions of MoS_2e are represented relative to vacuum level by considering the work function of both the S-termination (MoS_2e) and Se-termination (MoSeS). The band positions of the $\text{TiO}_2/\text{MoS}_2\text{e}$ and $\text{TiO}_2/\text{MoSeS}$ are represented using the work function of TiO_2 (Figure 3). The Fermi level is indicated with a black dashed line, and the vacuum level is set to zero.

built-in electric field pointing from MoS_2e to TiO_2 facilitates the charge separation and suppresses the recombination rate of charge carriers in the $\text{TiO}_2/\text{MoS}_2\text{e}$.⁶⁵ Moreover, the larger charge transfer can be attributed to the strong interlayer coupling and narrower interlayer distance, contributing to the larger amount of charge transferred from TiO_2 to MoS_2e .^{66,67} In the $\text{TiO}_2/\text{MoSeS}$ electrons were transferred in the opposite direction of the built-in electric field, which is proposed to contribute to reduce charge transfer across the interface. The Bader charges of the individual atoms in the isolated monolayers and heterostructures are provided in Figure S9 and S10, confirming the charge redistribution after constructing the heterostructures. The values support the strongest interaction between the closest O and S(Se) atoms at the interface. The small charge transfer across the interface

indicates relatively less chemical interaction between the TiO_2 and MoS₂ monolayers. In all, these results indicate that it is possible to construct stable heterostructures, out of lattice matching semiconductor monolayers and tune the electronic properties, according to varying interface terminations ranging from semiconducting to metallic.

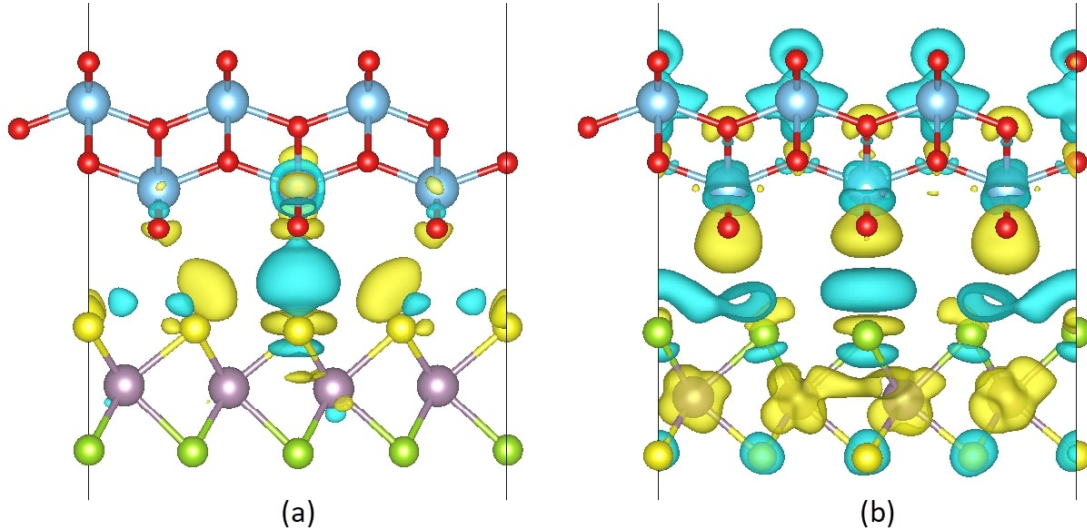


Figure 5: Charge density difference of the a) $\text{TiO}_2/\text{MoS}_2$ and b) $\text{TiO}_2/\text{MoSeS}$. The yellow isosurface refers to electron gain and blue refers to electron loss. The isosurface value is set to $0.003 e\text{\AA}^{-3}$.

Conclusions

We have investigated the structural and electronic properties of the $\text{TiO}_2/\text{MoS}_2$ and $\text{TiO}_2/\text{MoSeS}$ vdW heterostructures using first principles calculations. Both heterostructures were energetically stable, indicated by their negative formation energies. The band alignment was found to depend on the interface termination of MoS₂. The S termination at the interface led to a type II band alignment, providing efficient separation of photogenerated electrons and holes. The Se termination at the interface resulted in a type III band alignment and enabled a band-to-band tunneling of electrons across the interface. After forming the heterostructures electron transfer occurred from MoS₂ to TiO_2 . Interestingly, a built-in electric field was developed inside the heterostructures due to the difference in

the work functions of the TiO_2 and MoSSe layers, and that influenced the charge transfer at the interface. Our work demonstrates that the interface termination of MoSSe is a key factor in determining the properties of the TiO_2 -based vdW heterostructure. Tunability via changing the interface termination makes the heterostructure of 2D TiO_2 and MoSSe a potential candidate for various applications.

Acknowledgement

This work has received funding from the European Union's Horizon Europe research and innovation program under the Marie Skłodowska-Curie grant agreement no. 101081280, and the Finnish cultural foundation (Grant No. 00230235). CSC - IT Center for Science, Finland, is acknowledged for computational resources.

Declaration of competing interest

The authors declare no competing financial interests.

Supporting information

The supplementary material is hosted with the main article.

Description: Crystal structure of MoSSe and TiO_2 monolayers, different stacking configurations of TiO_2 and MoSSe monolayers, bond lengths in TiO_2 , band structure of MoSSe and TiO_2 , partial charge densities and partial density of states of $\text{TiO}_2/\text{MoSSe}$ and $\text{TiO}_2/\text{MoSeS}$, planar-averaged electrostatic potential of MoSSe and TiO_2 , and Bader charges in MoSSe and TiO_2 , and in $\text{TiO}_2/\text{MoSSe}$ and $\text{TiO}_2/\text{MoSeS}$.

References

- (1) Nguyen, T. T.; Patel, M.; Kim, S.; Mir, R. A.; Yi, J.; Dao, V.-A. Kim, J. Transparent photovoltaic cells and self-powered photodetectors by TiO₂/NiO heterojunction. *J. Power Sources* **2021**, *481*, 228865.
- (2) Aboulouard, A.; Gultekin, B.; Can, M.; Erol, M.; Jouatini, A.; Elhadadi, B.; Zafer, C.; Demic, S. Dye sensitized solar cells based on titanium dioxide nanoparticles synthesized by flame spray pyrolysis and hydrothermal sol-gel methods: a comparative study on photovoltaic performances. *J. Mater. Res. Technol.* **2020**, *9*, 1569.
- (3) Seh, Z. W.; Liu, S.; Low, M.; Zhang, S.-Y.; Liu, Z.; Mlayah, A.; Han, M.-Y. Janus Au-TiO₂ Photocatalysts with Strong Localization of Plasmonic Near-Fields for Efficient Visible-Light Hydrogen Generation. *Adv. Mater.* **2012**, *24*, 2310.
- (4) Han, F.; Kambala, V. S. R.; Srinivasan, M.; Rajarathnam, D.; Naidu, R. Tailored titanium dioxide photocatalysts for the degradation of organic dyes in wastewater treatment: a review. *Appl. Catal. A: Gen.* **2009**, *359*, 25.
- (5) Paul, S.; Rahman, M. A.; Sharif, S. B.; Kim, J.-H.; Siddiqui, S.-E.-T.; Hossain, M. A. M. TiO₂ as an Anode of High-Performance Lithium-Ion Batteries: A Comprehensive Review towards Practical Application. *Nanomaterials* **2022**, *12*, 2034.
- (6) Patra, J.; Wu, S.-C.; Leu, I.-C.; Yang, C.-C.; Dhaka, R. S.; Okada, S.; Yeh, H.-L.; Hsieh, C.-M.; Chang, B. K.; Chang, J. K. Hydrogenated Anatase and Rutile TiO₂ for Sodium-Ion Battery Anodes. *ACS Appl. Energy Mater.* **2021**, *4*, 5738.
- (7) Bhimanapati, G. R.; Li, Z.; Meunier, V.; Jung, Y.; Cha, J.; Das, S.; Xiao, D.; Son, Y.; Strano, M. S.; Cooper, V. R.; Liang, L.; Louie, S. G.; Ringe, R.; Zhou, W.; Kim, S. S.; Naik, R. R.; Sumpter, B. G.; Terrones, H.; Xia, F.; Wang, Y.; Zhu, J.; Akinwande, D.; Alem, N.; Schuller, J. A.; Schaak, R. E.; Terrones, M.; Robinson, J. A. Recent Advances in Two-Dimensional Materials beyond Graphene. *ACS Nano* **2015**, *9*, 11509.

- (8) Sasaki, T.; Watanabe, M. Macromolecule-like Aspects for a Colloidal Suspension of an Exfoliated Titanate. Pairwise Association of Nanosheets and Dynamic Reassembling Process Initiated from It. *J. Am. Chem. Soc.* **1996**, *118*, 8329.
- (9) Wang, L.; Wei, D.; Kang, S.; Xie, X.; Shi, Y. Two-Dimensional Titania: Structures and Properties Predicted by First Principle Calculation. *Phys. Chem. C* **2018**, *122*, 40.
- (10) Sakai, N.; Ebina, Y.; Takada, K.; Sasaki, T. Electronic Band Structure of Titania Semiconductor Nanosheets Revealed by Electrochemical and Photoelectrochemical Studies. *J. Am. Chem. Soc.* **2004**, *126*, 5851.
- (11) Kim, N.; Turner, E. M.; Kim, Y.; Ida, S.; Hagiwara, H.; Ishihara, T.; Ertekin, E. Two-Dimensional TiO₂ Nanosheets for Photo and Electro-Chemical Oxidation of Water: Predictions of Optimal Dopant Species from First-Principles. *J. Phys. Chem. C* **2017**, *121*, 19201.
- (12) Yuan, J.; Wang, C.; Liu, Y.; Wu, P.; Zhou, W. Tunable Photocatalytic HER Activity of Single-Layered TiO₂ Nanosheets with Transition-Metal Doping and Biaxial Strain. *J. Phys. Chem C* **2019**, *123*, 526.
- (13) Bellus, M. Z.; Li, M.; Lane, S. D.; Ceballos, F.; Cui, Q.; Zeng, X. C.; Zhao, H. Type-I van der Waals heterostructure formed by MoS₂ and ReS₂ monolayers. *Nanoscale* **2017**, *2*, 31.
- (14) Xu, T.; Wang, Y.; Zhou, X.; Zheng, X.; Xu, Q.; Chen, Z.; Ren, Y.; Yan, B. Fabrication and assembly of two-dimensional TiO₂/WO₃·H₂O heterostructures with type II band alignment for enhanced photocatalytic performance. *Appl. Surf. Sci.* **2017**, *403*, 564.
- (15) Bernardi, M. Palummo, M.; Grossman, J. C. Extraordinary Sunlight Absorption and One Nanometer Thick Photovoltaics Using Two-Dimensional Monolayer Materials. *Nano Lett.* **2013**, *13*, 3664.

- (16) Gong, C.; Zhang, H.; Wang, W.; Colombo, L. Wallace, R. M.; Cho, K. Band alignment of two-dimensional transition metal dichalcogenides: Application in tunnel field effect transistors. *Appl. Phys. Lett.* **2013**, *103*, 053513.
- (17) Fang, L.; Wang, T; Li, J.; Xia, C.; Li, X. Band structures and transport properties of broken-gap heterostructures: 2D C₃N/MX case. *Carbon* **2023**, *202*, 119.
- (18) Xuan, W.; Yang, N.; Luo, J.; Wang, R.; Yang, H.; Jin, G. Strain-modulated Rashba spin splitting and optical absorption of MoSSe/WSe₂ heterostructures. *Appl. Phys. A* **2023**, *129*, 88.
- (19) Zhou, B.; Jiang, K.; Shang, L.; Zhang, J. Li, Y.; Zhu, L.; Gong, S.-J.; Hu, Z.; Chu, J. Enhanced carrier separation in ferroelectric In₂Se₃/MoS₂ van der Waals heterostructure. *J. Mater. Chem. C* **2020**, *8*, 11160.
- (20) Cui, Z.; Bai, K.; Ding, Y.; Wang, X.; Li, E.; Zheng, J. Janus XSe/SiC (X = Mo, W) van der Waals heterostructures as promising water-splitting photocatalysts. *Physica E Low Dimens. Syst. Nanostruct.* **2020**, *123*, 114207.
- (21) Albar, A.; Aravindh, S. A. Emergence of metallic states at 2D MoSSe/GaAs Janus interface: a DFT study. *J. Phys. Condens. Matter* **2021**, *33*, 475701.
- (22) Lu, A.-Y.; Zu, H.; Xiao, J.; Chuu, C.-P.; Han, Y.; Chiu, M. H.; Cheng, C.-C.; Yang, C.-W.; Wei, K.-H.; Yang, Y.; Wang, Y.; Sokaras, D. Nordlund, D.; Yang, P.; Muller, D. A.; Chou, M.-Y.; Zhang, X.; Li, L.-J. Janus monolayers of transition metal dichalcogenides. *Nature Nanotech.* **2017**, *12*, 744.
- (23) Guo, S. D. Phonon transport in Janus monolayer MoSSe: a first-principles study. *Phys. Chem. Chem. Phys.* **2018**, *20*, 7236.
- (24) Peng, R.; Ma, Y.; Huang, B.; Dai, Y. Two-dimensional Janus PtSSe for photocatalytic water splitting under the visible or infrared light. *J. Mater. Chem. A* **2019**, *7*, 603.

- (25) Wang, C.; Chen, Y.-X.; Gao, G.; Shao, H. Theoretical investigations of Janus WSeTe monolayer and related Van der Waals heterostructures with promising thermoelectric performance. *Appl. Surf. Sci.* **2022**, *12*, 29335.
- (26) Ju, L.; Bie, M.; Tang, X.; Shang, J.; Kou, L. Janus WSSe Monolayer: An Excellent Photocatalyst for Overall Water Splitting. *ACS Appl. Mater. Interfaces* **2020**, *12*, 29335.
- (27) Vallinayagam, M.; Sudheer, A.E.; Aravindh, S. A.; Murali, D.; Raja, N.; Katta, R.; Posselt, M.; Zschornak, M. Novel Metalless Chalcogen-Based Janus Layers: A Density Functional Theory Study. *J. Phys. Chem. C* **2023**, *127*, 17029.
- (28) Zhao, y.; Zhang, H.; Cheng, X. A new type-II lepidocrocite-type TiO₂/GaSe heterostructure: Electronic and optical properties, bandgap engineering, interaction with ultrafast laser pulses. *arXiv:2102.04164 [cond-mat.mtrl-sci]*, **2021**.
- (29) Li, Y.; Cai, C.; Sun, B.; Chen, J. Novel electronic properties of 2D MoS₂/TiO₂ van der Waals heterostructure. *Semicond. Sci. Technol.* **2017**, *32*, 105011.
- (30) Sasaki, T.; Watanabe, M. Semiconductor Nanosheet Crystallites of Quasi-TiO₂ and Their Optical Properties. *J. Phys. Chem. B* **1997**, *101*, 10159.
- (31) Tran, K.; Moody, G.; Wu, F.; Lu, X.; Choi, J.; Kim, K.; Rai, A.; Sanchez, D. A.; Quan, J.; Singh, A.; Embley, J.; Zepeda, A.; Campbell, M.; Autry, T.; Taniguchi, T.; Watanabe, K.; Lu, N.; Banerjee, S. K.; Silverman, K. L.; Kim, S.; Tutuc, E.; Yang, L.; MacDonald, A. H.; Li, X. Evidence for moiré excitons in van der Waals heterostructures. *Nature* **2019**, *567*, 71.
- (32) Kresse, G.; Hafner, J. Ab initio molecular dynamics for liquid metals. *Phys. Rev. B* **1993**, *47*, 558.
- (33) Kresse, G.; Furthmüller, J. Efficiency of ab-initio total energy calculations for metals and semiconductors using a plane-wave basis set. *Comput. Mater. Sci.* **1996**, *6*, 15.

- (34) Kresse, G.; Furthmüller, J. Efficient iterative schemes for ab initio total-energy calculations using a plane-wave basis set. *Phys. Rev. B* **1996**, *54*, 11169.
- (35) Kresse, G.; Joubert, D. From ultrasoft pseudopotentials to the projector augmented-wave method. *Phys. Rev. B* **1999**, *59*, 1758.
- (36) Blöchl, P. E. Projected augmented-wave method. *Phys. Rev. B* **1994**, *50*, 17953.
- (37) Perdew, J. P.; Burke, K.; Ernzerhof, M. Generalized Gradient Approximation Made Simple. *Phys. Rev. Lett.* **1996**, *77*, 3865.
- (38) Kumaravel, V.; Rhatigan, S.; Mathew, S.; Bartlett, J.; Nolan, M.; Hinder, S. J.; Sharma, P. K.; Singh, A.; Bryne, J. A.; Harrison, J.; Pillai, S. C. Indium-Doped TiO₂ Photocatalysts with High-Temperature Anatase Stability. *J. Phys. Chem. C* **2019**, *123*, 21083.
- (39) Dudarar, S. L.; Botton, G. A.; Savrasov, S. Y.; humphreys, C. J.; Sutton, A. P. Electron-energy-loss spectra and the structural stability of nickel oxide: An LSDA+U study. *Phys. Rev. B: Condens. Matter Mater. Phys.* **1998**, *57*, 1505.
- (40) Tkatchenko, A.; Scheffler, M. Accurate Molecular Van Der Waals Interactions from Ground-State Electron Density and Free-Atom Reference Data. *Phys. rev. Lett.* **2009**, *102*, 073005.
- (41) Monkhorst, H. J.; Pack, J. D. Special points for Brillouin-zone integrations. *Phys. Rev. B* **1976**, *13*, 5188.
- (42) Momma, K.; Izumi, F. VESTA: a three-dimensional visualization system for electronic and structural analysis. *J. Appl. Cryst.* **2008**, *41*, 653.
- (43) Wang, V.; Xu, N.; Liu, J. C.; Tang, G.; Geng, W. T. VASPKIT: A user-friendly interface facilitating high-throughput computing and analysis using VASP code. *Comput. Phys. Commun.* **2021**, *267*, 108033.

- (44) Kang, J.; Li, J.; Li, S.-S.; Xia, J.-B.; Wang, L.-W. Electronic Structural Moiré Pattern Effects on MoS₂/MoSe₂ 2D Heterostructures. *Nano Lett.* **2013**, *13*, 5485.
- (45) Wen, Y.-N.; Xia, M.-G.; Zhang, S.-L. Bandgap engineering of Janus MoSSe monolayer implemented by Se vacancy. *Comput. Mater. Sci.* **2018**, *152*, 20.
- (46) Zhou, W.; Umezawa, N.; Ma, R.; Sakai, N.; Ebina, Y.; Sano, K.; Liu, M.; Ishida, Y.; Aida, T.; Sasaki, T. Spontaneous Direct Band Gap, High Hole Mobility, and Huge Exciton Energy in Atomic-Thin TiO₂ Nanosheet. *Chem. Mater.* **2018**, *30*, 6449.
- (47) Wang, S.L.; Luo, X.; Zhou, X.; Zhu, Y.; Chi, X.; Chen, W.; Wu, K.; Liu, Z.; Quek, S.-Y.; Xu, G.-Q. Fabrication and Properties of a Free-standing Two-Dimensional Titania, *J. Am. Chem. Soc.* **2017**, *139*, 15414.
- (48) Wang, Y.; Chen, R.; Luo, X.; Liang, Q.; Wang, Y.; Xie, Q. First-Principles Calculations on Janus MoSSe/Graphene van der Waals Heterostructures: Implications for Electronic Devices. *ACS Appl. Nano Mater.* **2022**, *5*, 8371.
- (49) Wang, P.; Jia, C.; Huang, Y.; Duan, X. Van der Waals Heterostructures by Design: From 1D and 2D to 3D. *Matter* **2021**, *4*, 552.
- (50) Pushkarev, G. V.; Mazurenko, V. G.; Mazurenko V. V.; Boukhvalov, D. W. Nature of Interlayer Bonds in Two-Dimensional Materials. *J. Phys. Chem. C.* **2023**, *127*, 8148.
- (51) Din, H. U.; Idrees, M.; Albar, A.; Shafiq, M.; Agmad, I.; Nguyen, C. V.; Amin, B. Rashba spin splitting and photocatalytic properties of GeC-MSSe (M = Mo, W) van der Waals heterostructures. *Phys. Rev. B.* **2019**, *100*, 165425.
- (52) Zhou, W.; Chen, J.; Yang, Z.; Liu, J.; Ouyang, F. Geometry and electronic structure of monolayer, bilayer, and multilayer Janus WSSe. *Phys. Rev. B* **2019**, *99*, 075160.
- (53) Tang, Y.; Liu, Q.; Lei, J.; Zhang, M.; Yang, H.; Duan, M.; Ma, X.; Song, T. MoS₂/TiO₂

- van der Waals heterostructures for promising photocatalytic performance: a first-principles study. *Mater. Res. Express* **2022**, *9*, 105502.
- (54) Mao, X.; Li, J.; Liu, Z.; Wang, G.; Zhang, Q.; Jin, Y. T-Phase and H-Phase Coupled TMD van der Waals Heterostructure ZrS₂/MoTe₂ with Both Rashba Spin Splitting and Type-III Band Alignment. *J. Phys. Chem. C* **2022**, *126*, 10601.
- (55) Li, S.; Sun, M.; Chou, J.-P.; Wei, J.; Xing, H.; Hu, A. First-principles calculations of the electronic properties of SiC-based bilayer and trilayer heterostructures. *Phys. Chem. Chem. Phys.* **2018**, *20*, 24726.
- (56) Entani, S.; Antipina, L. Y.; Avramov, P. V.; Ohtomo, M.; Matsumoto, Y.; Hirao, N.; Shimoyama, I.; Naramoto, H.; Bada, Y.; Sorokin, P. B.; Sakai, S. Contracted Interlayer Distance in Graphene/Sapphire Heterostructure. *Nano Res.* **2015**, *8*, 1535.
- (57) Ahmad, W.; Liu, J.; Jiang, J.; Hao, Q.; Wu, D.; Ke, Y.; Gan, H.; Laxmi, V.; Ouyang, Z.; Ouyang, F.; Wang, Z.; Liu, F.; Qi, D.; Zhang, W. Strong Interlayer Transition in Few-Layer InSe/PdSe₂ van der Waals Heterostructure for Near-Infrared Photodetection. *Adv. Funct. Mater.* **2021**, *31*, 2104143.
- (58) Yan, R.; Fathipour, S.; Yimo, H.; Song, B.; Xiao, S.; Li, M.; Ma, M.; Protasenko, V.; Muller, D.-A.; Jena, D.; Xing, H.-G. Esaki Diodes in van der Waals Heterojunctions with Broken-Gap Energy Band Alignment. *Nano Lett.* **2015**, *15*, 5791.
- (59) Xia, C.; Du, J.; Li, M.; Li, X.; Zhao, X.; Wang, T. Li, J. Effects of Electric Field on the Electronic Structures of Broken-gap Phosphorene/SnX₂ (X = S, Se) van der Waals Heterojunctions. *Phys. Rev. Appl.* **2018**, *10*, 054064.
- (60) Kim, K.-H.; Park, H.-Y.; Shim, J.; shin, G.; reev, M.; Koo, J.; yoo, G.; Jung, K.; Heo, Y.; Yu, H.-Y.; Kim, K. R.; Cho, J. H.; Lee, S.; Park, J.-H. A multiple negative differential resistance heterojunction device and its circuit application to ternary static random access memory. *Nanoscale Horiz.* **2020**, *5*, 654.

- (61) Zhou, Z.; Niu, X.; Zhang, Y.; Wang, J. Janus MoSSe/WSeTe heterostructures: a direct Z-scheme photocatalyst for hydrogen evolution. *J. Mater. Chem. A* **2019**, *7*, 21835.
- (62) Li, X.; Wang, X.; Hao, W.; Mi, C.; Zhou, H. Structural, electronic, and electromechanical properties of MoSSe/blue phosphorene heterobilayer. *AIP Advances* **2019**, *9*, 115302.
- (63) Zhang, K.; Guo, Y.; Larson, D. T.; Zhu, Z.; Fang, S.; Kaxiras, E.; Kong, J.; Huang, S. Spectroscopic Signatures of Interlayer Coupling in Janus MoSSe/MoS₂ Heterostructures. *ACS Nano* **2021**, *15*, 14394.
- (64) Yu, S.; Wei, W.; Li, F.; Huang, B.; Dai, Y. Electronic properties of Janus MXY/graphene (M = Mo, W; X ≠ Y = S, Se) van der Waals structures: a first-principles study. *Phys. Chem. Chem. Phys.* **2020**, *22*, 25675.
- (65) Shokri, A.; Yazdani, A. Band alignment engineering, electronic and optical properties of Sb/PtTe₂ van der Waals heterostructure: effects of electric field and biaxial strain. *J. Mater. Sci.* **2021**, *56*, 5658.
- (66) Xu, L.; Huang, W.-Q.; hu, W.; Yang, K.; Zhou, B.-X.; Pan, A.; Huang, G.-F. Two-Dimensional MoS₂-Graphene-Based Multilayer van der Waals Heterostructures: Enhanced Charge Transfer and Optical Absorption, and Electric-Field Tunable Dirac Point and Band Gap. *Chem. Mater.* **2017**, *29*, 5504.
- (67) Fang, Q.; Li, M.; Zhao, X.; Yuan, L.; Wang, B.; Xia, C.; Ma, F. van der Waals graphene/MoS₂ heterostructures: tuning the electronic properties and Schottky barrier by applying a biaxial strain. *Mater. Adv.* **2022**, *3*, 624.
- (68) Wang, S.; Tian, H.; Ren, C.; Yu, J.; Sun, M. Electronic and optical properties of heterostructures based on transition metal dichalcogenides and graphene-like zinc oxide. *Sci. Rep.* **2018**, *8*, 12009.

- (69) Cai, Y.; Zhang, G.; Zhang, Y.-W. Electronic Properties of Phosphorene/Graphene and Phosphorene/Hexagonal Boron Nitride Heterostructures. *J. Phys. Chem. C* **2015**, *119*, 13929.
- (70) Tang, W.; Sanville, E.; Henkelman, G. A grid-based Bader analysis algorithm without lattice bias. *J. Phys.: Condens. Matter* **2009**, *21*, 084204.

Supplementary information

Tuning the Electronic Properties of Two-Dimensional Lepidocrocite Titanium Dioxide Based Heterojunctions

Kati Asikainen^{†,*}, Matti Alatalo[†], Marko Huttula[†], and S. Assa Aravindh^{†,*}

[†]*Nano and Molecular Systems Research Unit, University of Oulu, FI-90014, Finland*

E-mail: Kati.Asikainen@oulu.fi; Assa.SasikalaDevi@oulu.fi

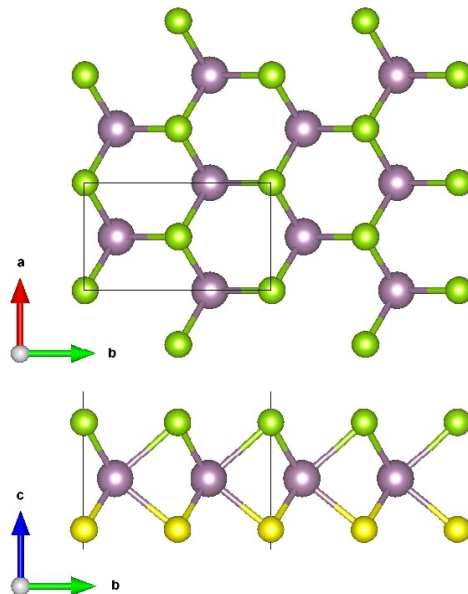


Figure S1: Rectangular unit cell of 2D MoSSe with a unit cell size of $a = 3.25 \text{ \AA}$ and $b = 5.64 \text{ \AA}$.

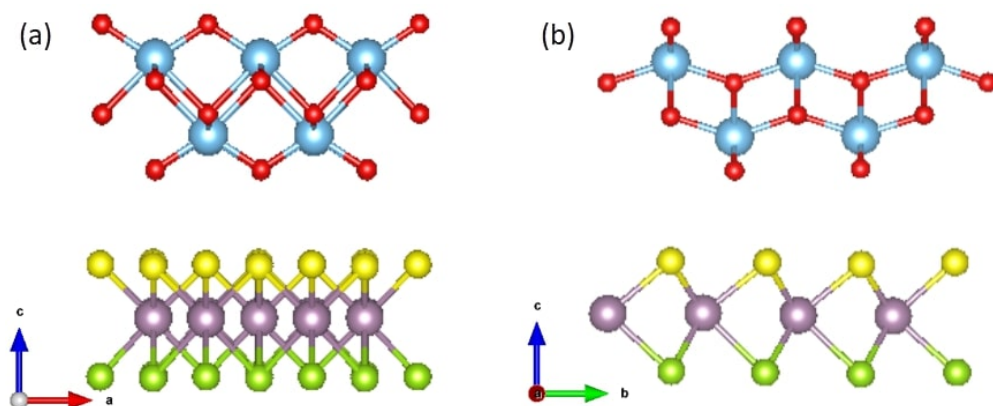


Figure S2: Stacking configuration of 2D lepidocrocite-type TiO_2 and 2D MoSSe monolayers along the a) x-direction and b) y-direction. According to Li *et al.* the particular stacking configuration of 2D TiO_2 and MoS_2 is the most stable.¹

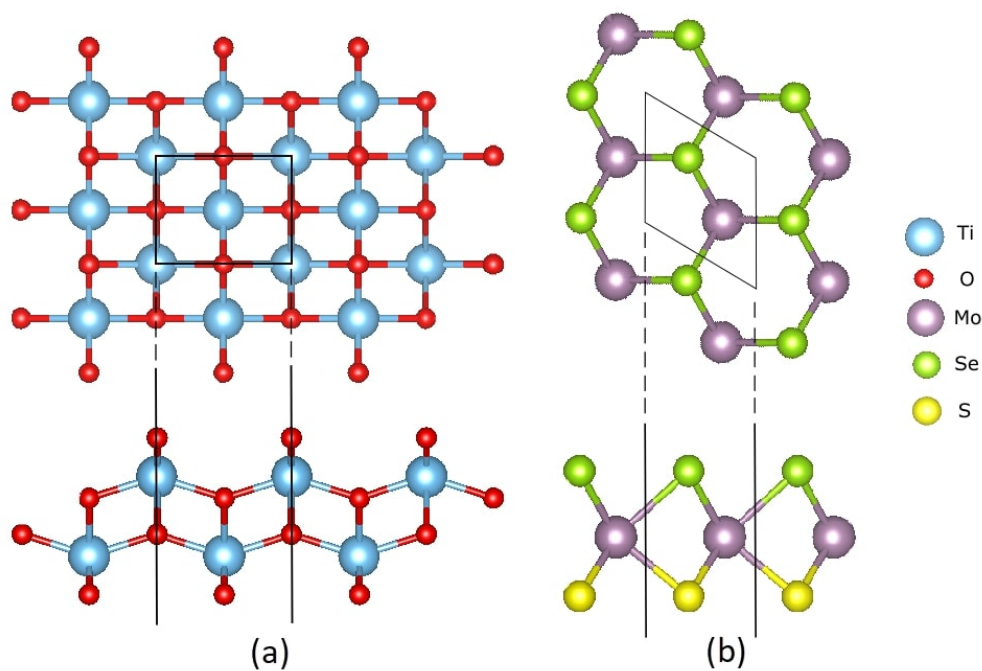


Figure S3: Top (upper) and side (lower) view of the a) 2D lepidocrocite-type TiO_2 and b) 2D MoSSe . The primitive unit cells are indicated with black lines.

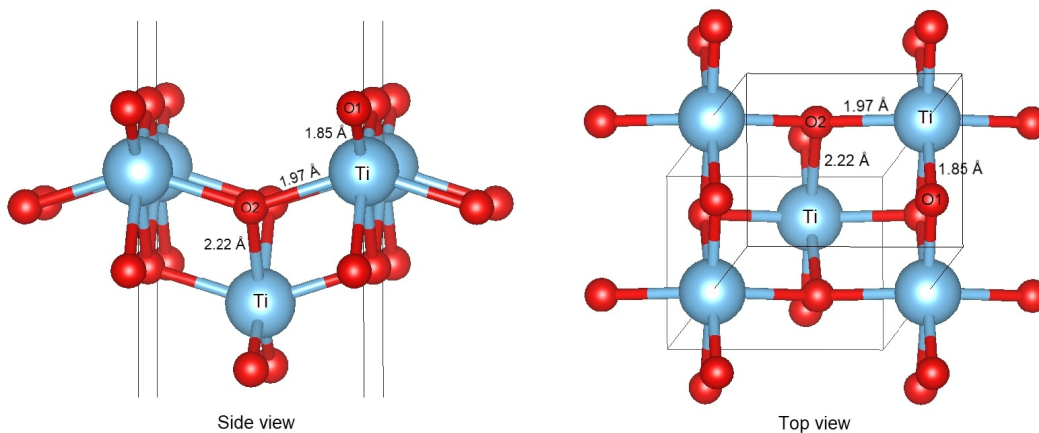


Figure S4: The optimized structure of 2D lepidocrocite-type TiO_2 . The monolayer consists of two-fold (O1) and four-fold (O2) oxygen atoms, and six-fold titanium (Ti) atoms. The Ti-O1 bond lengths were found to be 1.85 Å, and the two different Ti-O2 bonds were 1.97 Å and 2.22 Å, being in agreement with reported values.^{2,3}

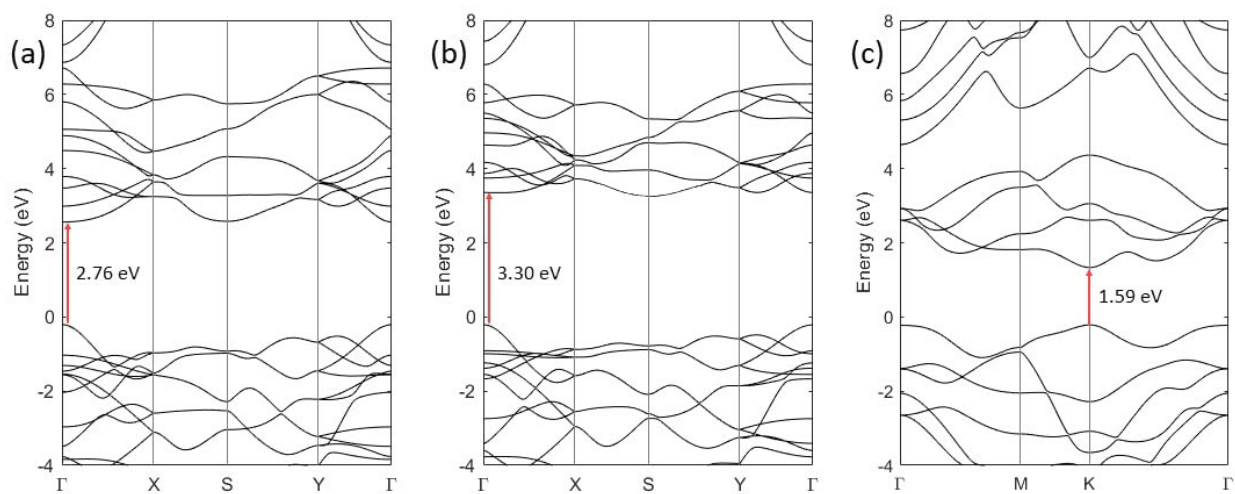


Figure S5: Band structure of 2D TiO_2 using the a) GGA and b) GGA+U functional. A direct band gap of 2.76 eV and 3.30 eV were found, respectively. For c) MoSSE we found a direct band gap of 1.59 eV using the GGA functional. Band gap is indicated with a red arrow in the plots.

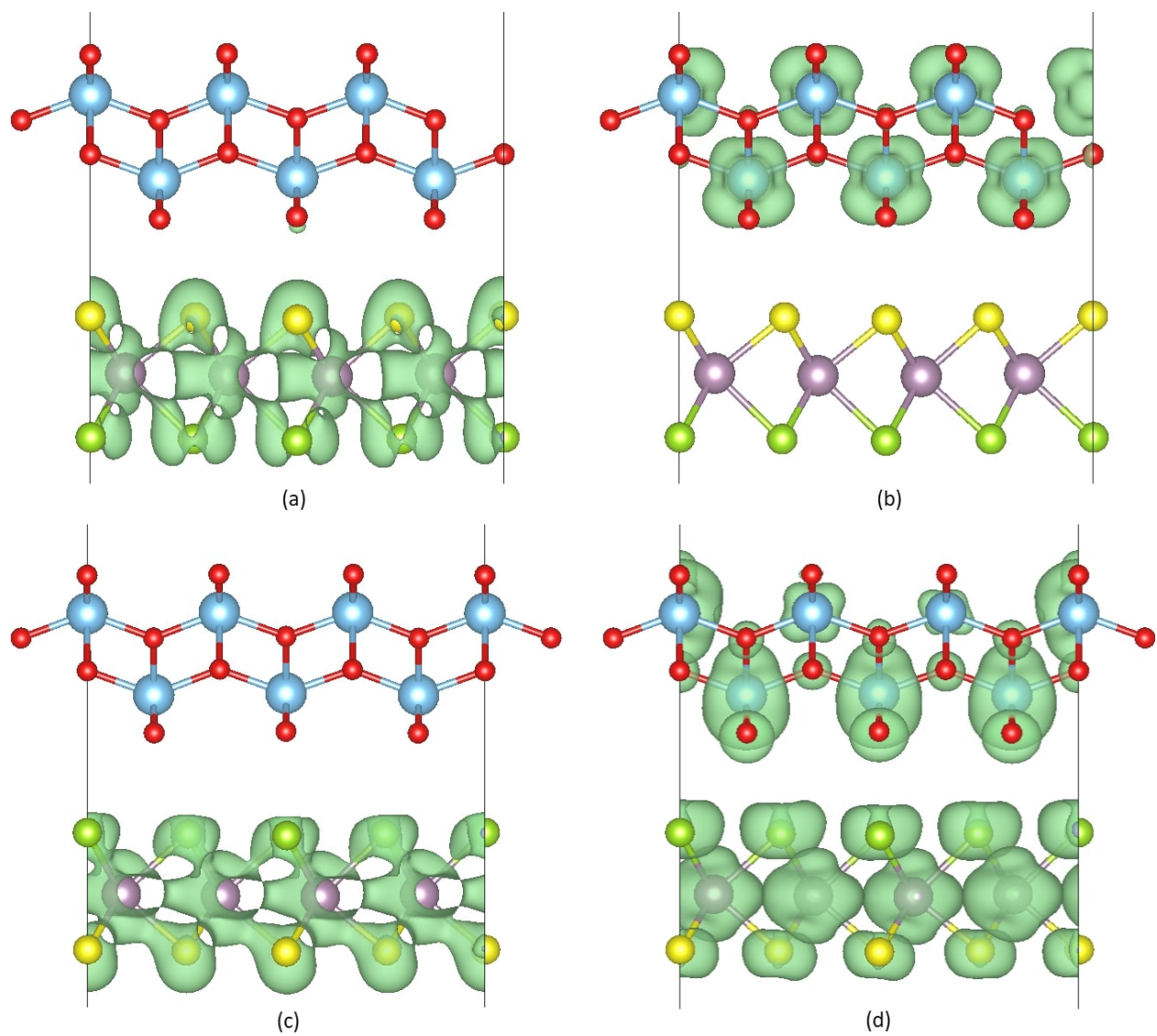


Figure S6: Decomposed charge densities of the VBM and CBM of the $\text{TiO}_2/\text{MoSSe}$ (a and b) and $\text{TiO}_2/\text{MoSeS}$ (c and d). Isosurface value is set to $0.006 e\text{\AA}^{-3}$.

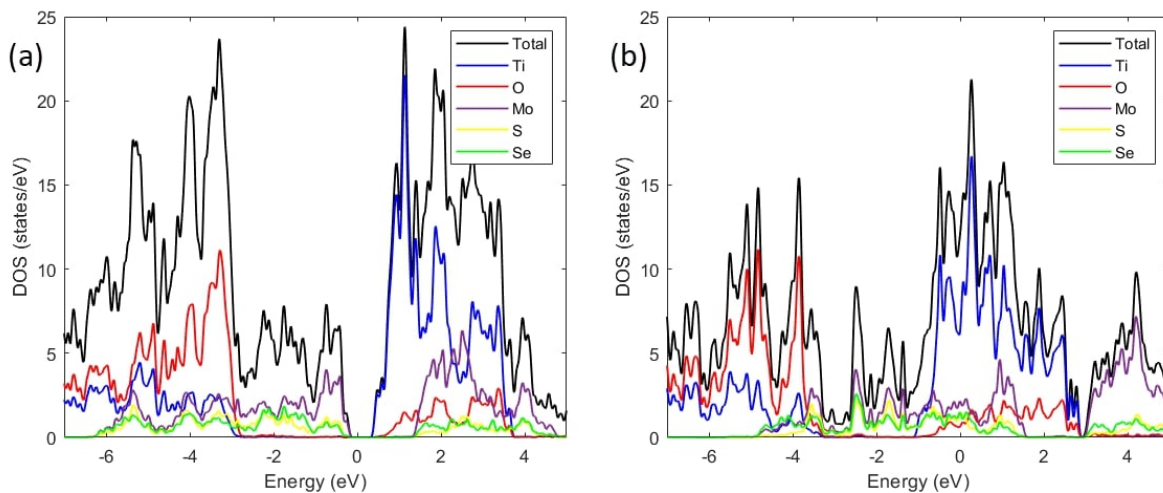


Figure S7: Partial density of states of Ti, O, Mo, S and Se in the a) $\text{TiO}_2/\text{MoSSe}$ and b) $\text{TiO}_2/\text{MoSeS}$ heterostructures.

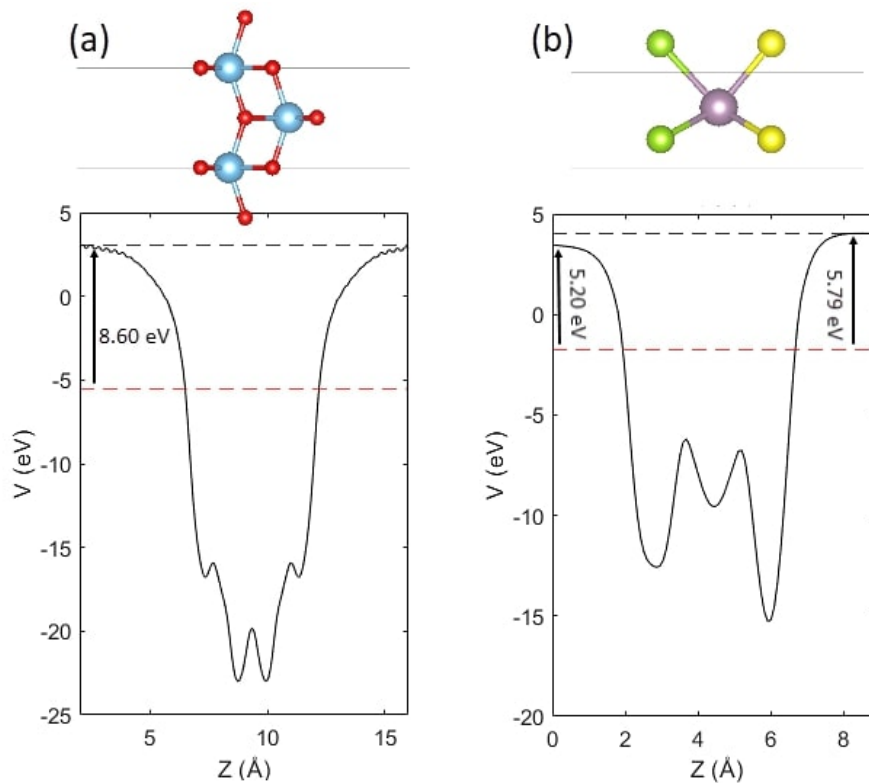


Figure S8: Planar-averaged electrostatic potential of the a) TiO_2 and b) MoSSe monolayers.

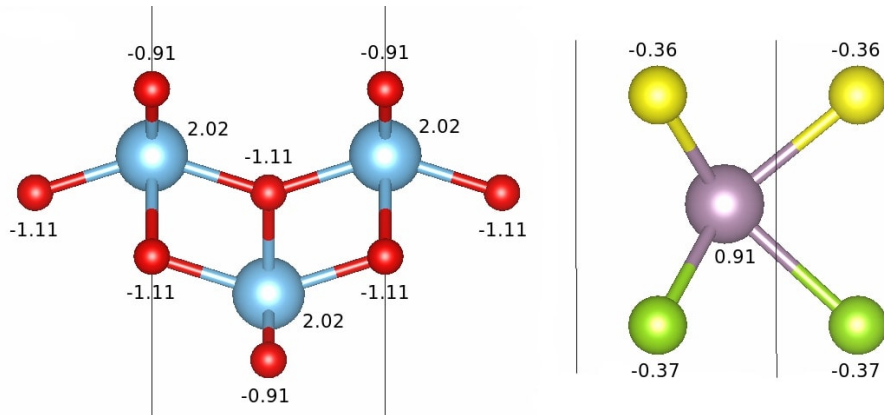


Figure S9: Bader charges of the atoms in the free-standing a) TiO_2 and b) MoS_2 monolayers. Positive value refers to electron loss and negative value to electron gain. In the TiO_2 Ti atoms give $2.02 e$ for covalent bonding while two-fold and four-fold oxygen atoms gain $-0.91 e$ and $-1.11 e$ per unit cell, respectively. In the MoS_2 Mo atom exhibits a loss of charge which is accumulated to S and Se sites.

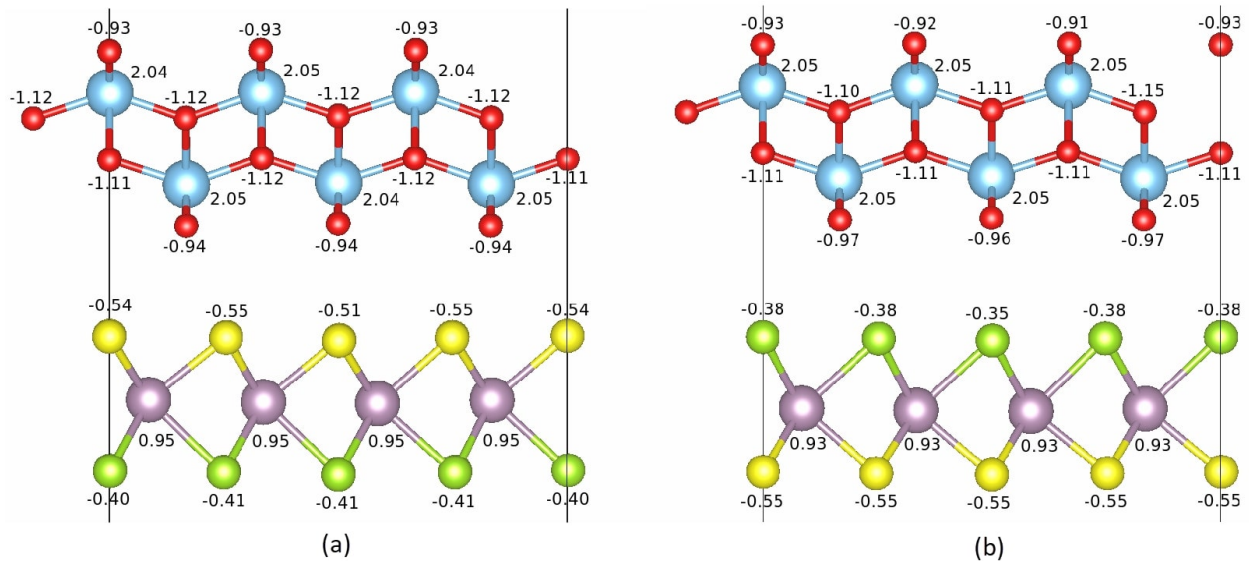


Figure S10: Bader charges of the atoms in the a) $\text{TiO}_2/\text{MoS}_2$ and b) $\text{TiO}_2/\text{MoSeS}$ after constructing the heterostructures. The charge redistribution occurs in both monolayers. At the interface the Bader charges of O atoms and S (Se) atoms vary, showing the strongest interaction between the closest O and S (Se) atoms.

References

- (1) Li, Y.; Cai, C.; Sun, B.; Chen, J. Novel electronic properties of 2D MoS₂ /TiO₂ van der Waals heterostructure. *Semicond. Sci. Technol.* **2017**, *32*, 105011.
- (2) Sato, H.; Oto, K.; Sasaki, T.; Yamagishi, A. First-Principles Study of Two-Dimensional Titanium Dioxides. *J. Phys. Chem. B* **2003**, *107*, 9824 .
- (3) Zhao, Y.; Zhang, H; Cheng, X., A new type-II lepidocrocite-type TiO₂/GaSe heterostructure: Electronic and optical properties, bandgap engineering, interaction with ultrafast laser pulses. *arXiv:2102.04164 [cond-mat.mtrl-sci]* **2021**.